Supplementary Information:

Antenna-electrodes for controlling electroluminescence

Kevin C. Y. Huang, Min-Kyo Seo*, Yijie Huo, Tomas Sarmiento,
James S. Harris and Mark L. Brongersma*

Supplementary Figures

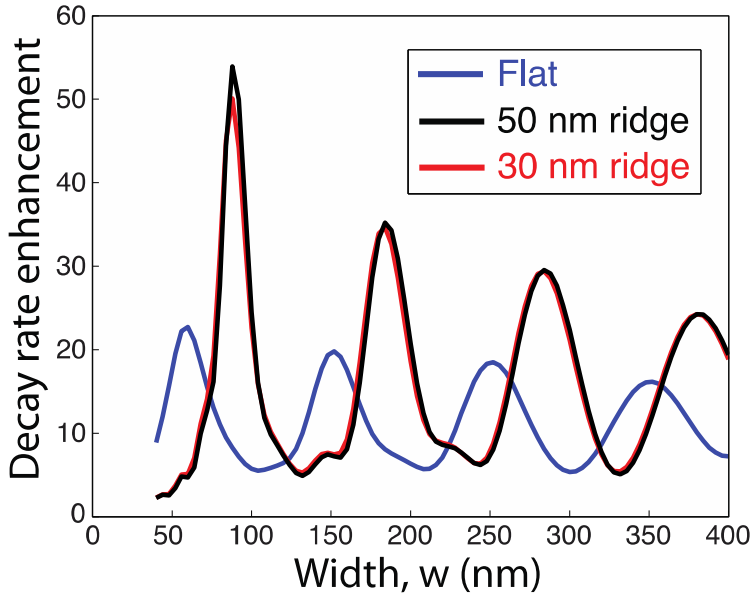

Supplementary Figure S1: 2D FDTD modeling of decay rate enhancements as a function of antenna widths. All 3 curves are for a vertical dipole placed 10 nm underneath the edge of the antenna. Both the 30-nm- and 50-nm-tall ridge structures (red and black) show approximately two times enhancement over the flat geometry (blue) of the same resonance order due to the stronger transverse SPP resonance. The resonance widths for both flat and ridge geometries match the 3D simulations (±5 nm), confirming the equivalence of 2D and 3D simulations in the XZ-plane. Furthermore, the ridge structures exhibit higher decay rate enhancement as well as larger oscillation amplitude as a function of antenna width, indicating stronger resonance of SPPs propagating in the x-direction compared to the flat geometry. Thus, the QW ridge structure not only provides carrier confinement, but also better optical confinement for SPPs. Note the difference between 30-nm- and 50-nm-tall ridge is negligible due to the small mode size of less than 60 nm.

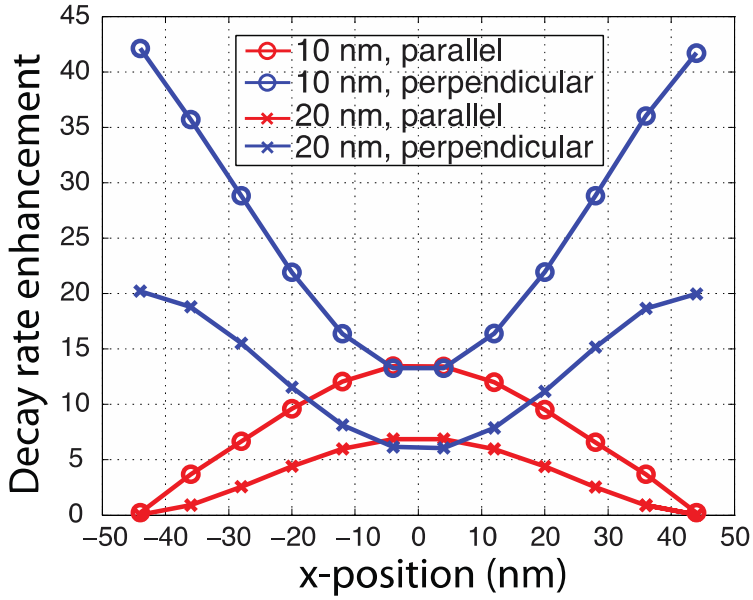

Supplementary Figure S2: Spatial variation of decay rate enhancements calculated in 3D FDTD. Decay rate enhancements as a function of x-position for perpendicular (blue) and parallel (red) dipoles placed 10 nm (circle) or 20 nm (cross) beneath a 90-nm-wide antenna on 50-nm-tall QW ridge. As expected by considering the electric field mode profile for the lowest order stripe antenna resonance, the enhancements for perpendicular dipoles maximize at the two ends of the stripe while the parallel dipole enhancements maximize at the center. For all positions, dipoles placed closer to the Au-GaAs surface experience greater enhancements due to stronger coupling to SPPs and lossy waves. The spatially and polarization averaged decay rate enhancements for 10 nm and 20 nm spacer thicknesses are 17 and 8.4 respectively which are approximately 1.5 times higher than the case for a planar Au film on GaAs.

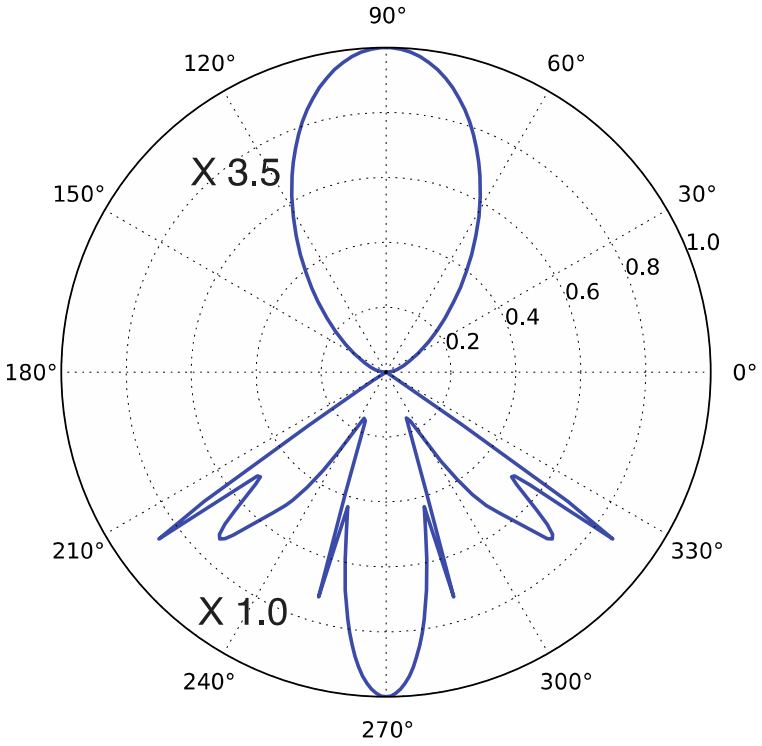

Supplementary Figure S3: Calculated polar radiation pattern for the 290-nm-wide antenna. The ensemble upper hemisphere air emission pattern is single lobed, while the substrate emission exhibits several narrow emission peaks. Due to the angular resolution limit of the plot, actual peak emission intensity into the substrate is in fact larger than displayed.

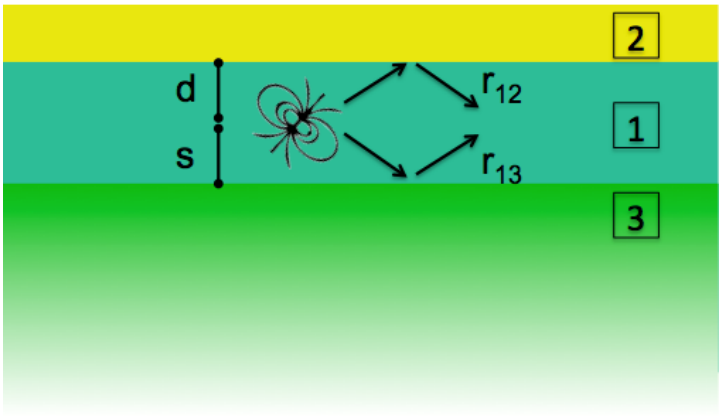

Supplementary Figure S4: Schematic of an electric dipole radiating in a planar stack. Each medium is numbered from 1 to 3. The reflection coefficients are defined for waves propagating from medium 1 to medium 2 and 3. The oscillating dipole is placed in medium 1. *d* is the distance from the dipole to the interface between medium 1 and medium 2, *s* is the distance from the dipole to the interface between medium 1 and medium 2. In our example where an emitter in GaAs is placed underneath a layer of 20 nm thick Au film, both medium 1 and 3 are modeled as GaAs and layer 2 is specified to be Au.

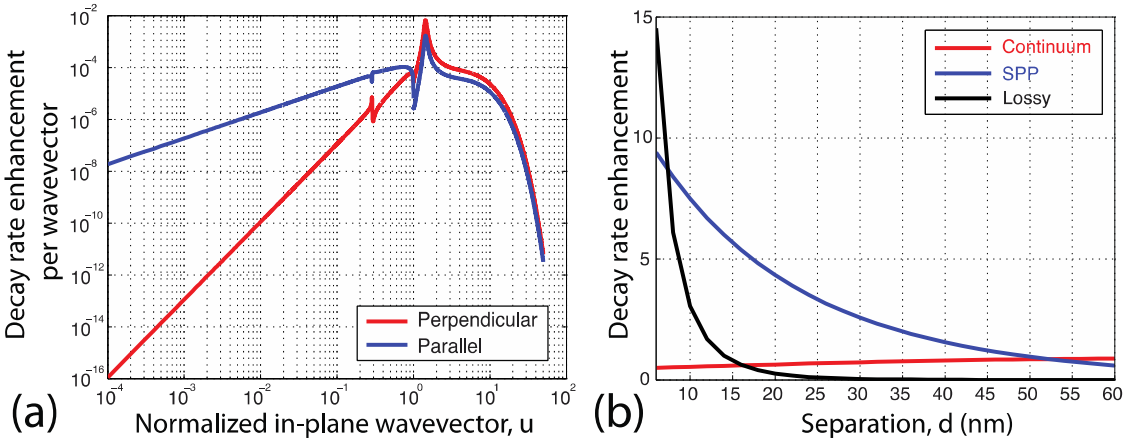

Supplementary Figure S5: Separation of decay channels in terms of normalized in-plane wavevectors. a, decay rate enhancement per wavevector as a function of normalized in-plane wavevector for parallel and perpendicular dipoles placed 10 nm below the Au surface . $u \approx 0.3$ is the cut-off for propagating waves in air and $u=1$ is the cut-off for propagating waves in GaAs, near each of which a discontinuity in the decay rate enhancements is observed. The peak just above $u=1$ corresponds to SPP excitation, while the shoulder above $u=3$ is the lossy wave contributions. Using these definitions, we calculate the decay rate enhancement for each channel (propagating continuum, SPP, lossy waves) as a function of emitter-Au separation for a randomly oriented dipole where we weigh the decay rate enhancement for the parallel dipole by 2/3 and the vertical dipole by 1/3. **b,** contributions to the total decay rate enhancement as a function of emitter-Au separation for a randomly polarized dipole.

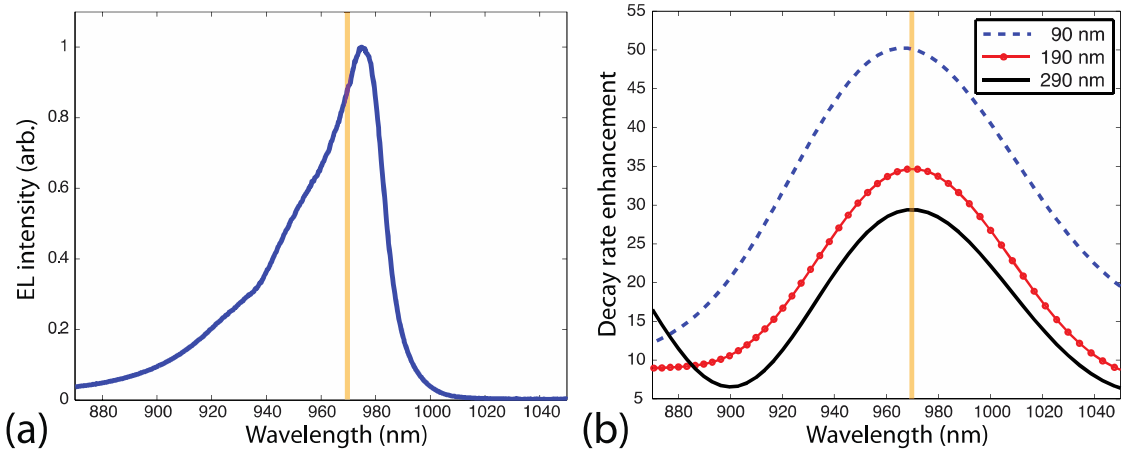

Supplementary Figure S6: QW EL spectrum and stripe antenna bandwidth. a, Measured room-temperature EL spectrum for a planar large-area $In_{0.16}Ga_{0.84}As$/GaAs QW. The peak emission wavelength is centered at 975 nm. The asymmetric spectrum is characteristic of QW emission where the EL intensity drops off sharply for energies below the lowest state in the QW and the tail at higher energies is due to the combined effects of the electronic density of states and the Fermi-Dirac distribution function. **b,** Calculated decay rate enhancement spectrum for a vertical dipole placed 10 nm beneath the end of stripe antennas supporting the first, second and third (90 nm, 190 nm, 290 nm) SPP resonances using 2D FDTD. The orange vertical lines in **a** and **b** indicate the wavelength used in all other numerical analysis. Due to the low radiation Q of the stripe antennas, all three resonances are broader than the emission spectrum. For this reason, No significant modification of the emission spectrum is expected due to the presence of the antenna. Furthermore, the interaction between the QW and the antenna can be treated as emission coupling to a single antenna SPP resonance (i.e. the relatively narrow EL bandwidth cannot simultaneous excite more than one antenna SPP resonance order).

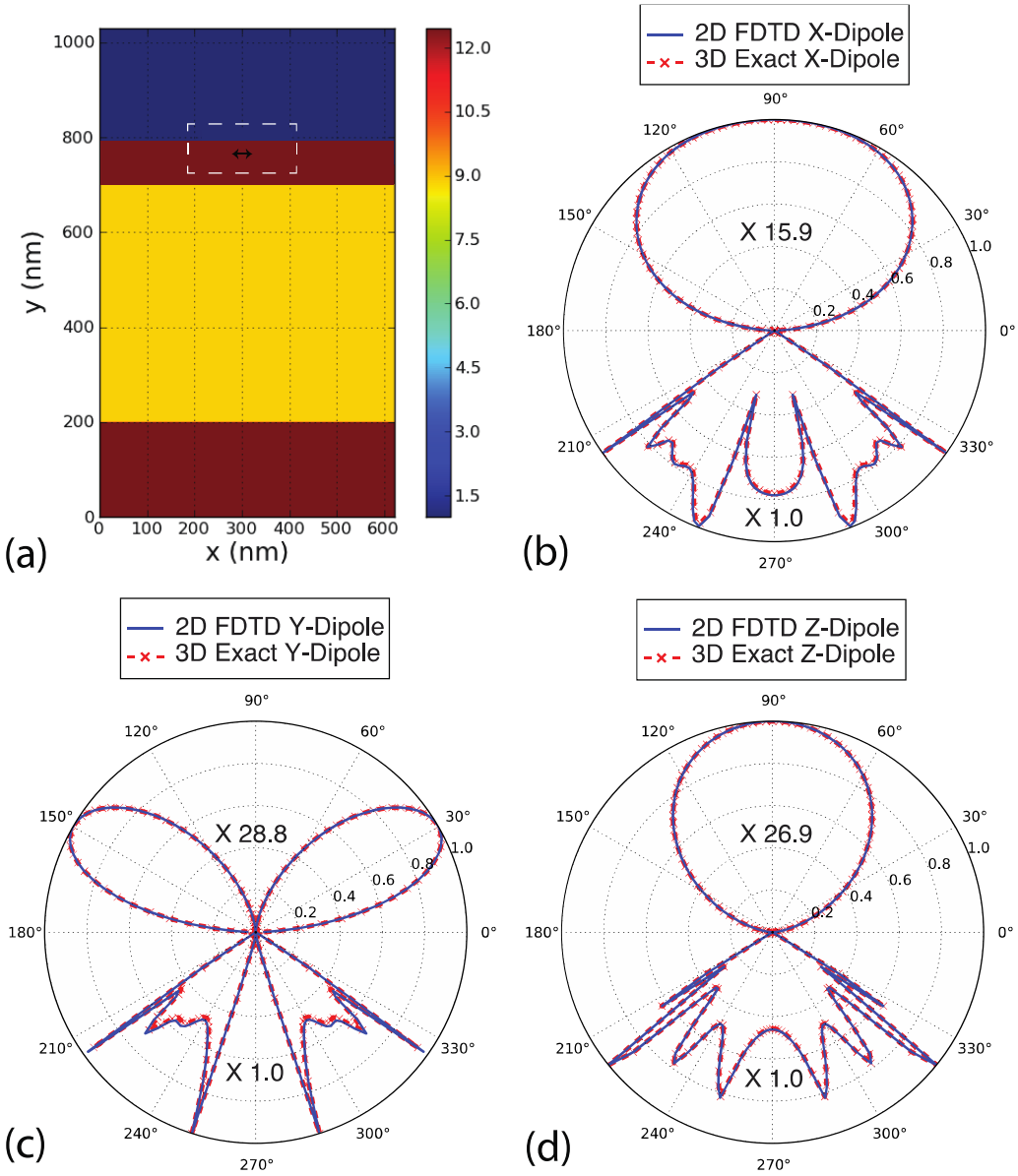

Supplementary Figure S7: Comparison of 2D FDTD dipole NTFF with exact infinitesimal dipole far-field on a substrate. a, Map of 2D FDTD simulation relative permittivity. White dashed line indicates the equivalence current surface. The arrow indicates the position of the point dipole 10 nm beneath the air/ GaAs interface with a polarization of X, Y or Z. **b,** Comparison of the far-field radiation pattern of a 2D FDTD simulated X-dipole and the exact analytical infinitesimal 3D X-dipole. **c,** Comparison of the far-field radiation pattern of a 2D FDTD simulated Y-dipole and the exact analytical infinitesimal 3D Y-dipole. **d,** Comparison of the far-field radiation pattern of a 2D FDTD simulated Z-dipole and the exact analytical

infinitesimal 3D Z-dipole. The air and substrate emission are separately normalized to their maximum values in order to bring attention to the peak emission angles and the shape of the lobes rather than the relative strengths of the emission. The corresponding multiplication factors are indicated in the corresponding hemispheres.

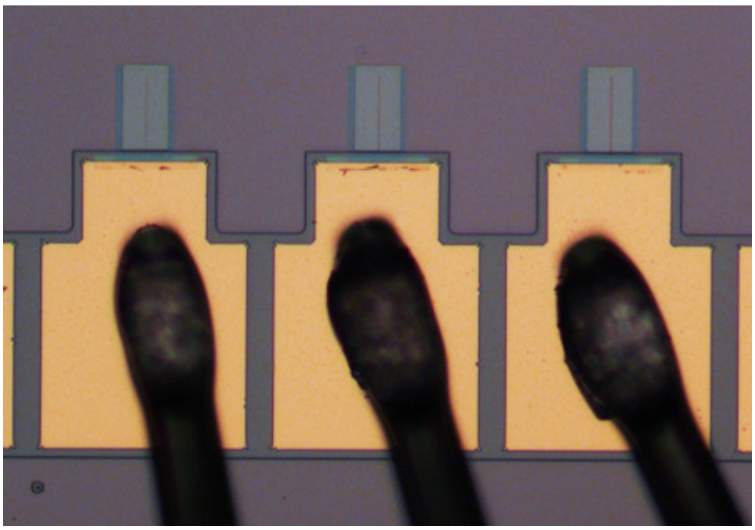

Supplementary Figure S8: Optical microscope image of separately wirebonded devices.

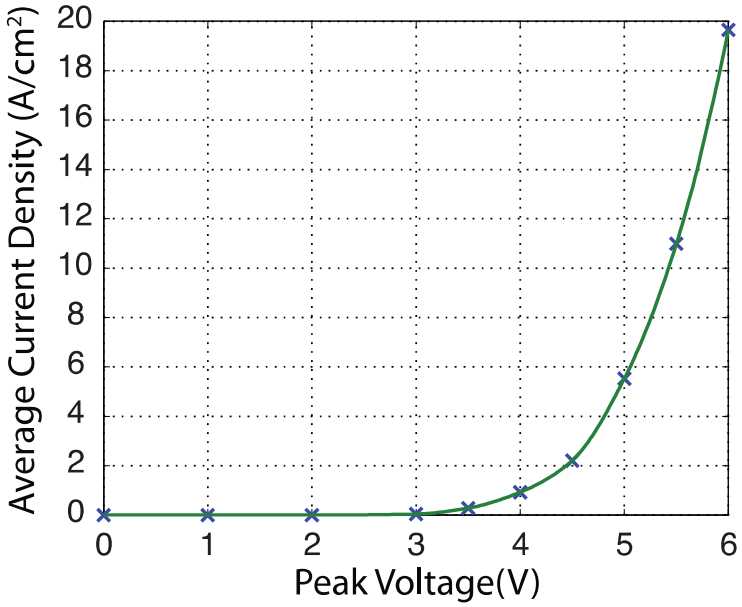

Supplementary Figure S9: Average current density V.S. pulsed peak voltage. The device IV characteristics under the same pulsed voltage excitation (2MHz repetition rate, 10 ns pulse width) as the EL measurements.

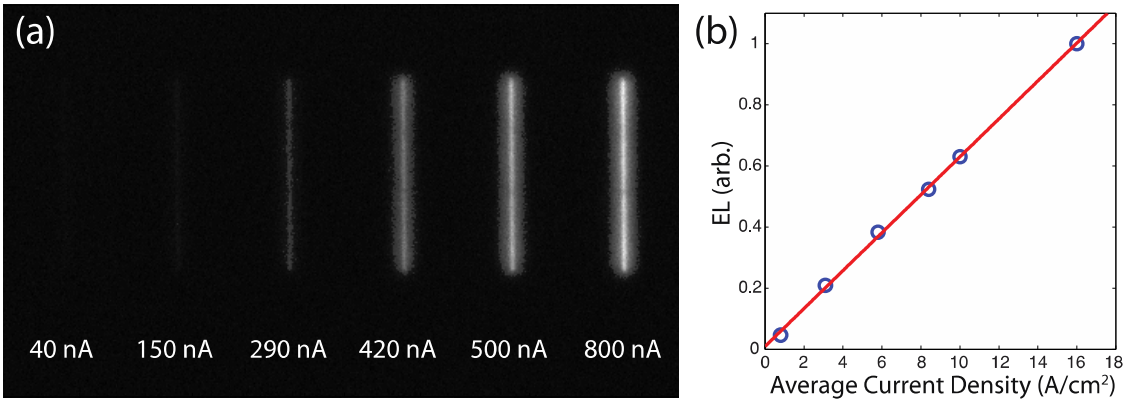

Supplementary Figure S10: Typical antenna-electrode driven EL versus average current characteristics. a, Optical microscope images of the EL for the same device under increasing driving current. **b,** Total integrated EL intensity along the antenna-electrode as a function of average current density. The red line shows the linear fitting curve.

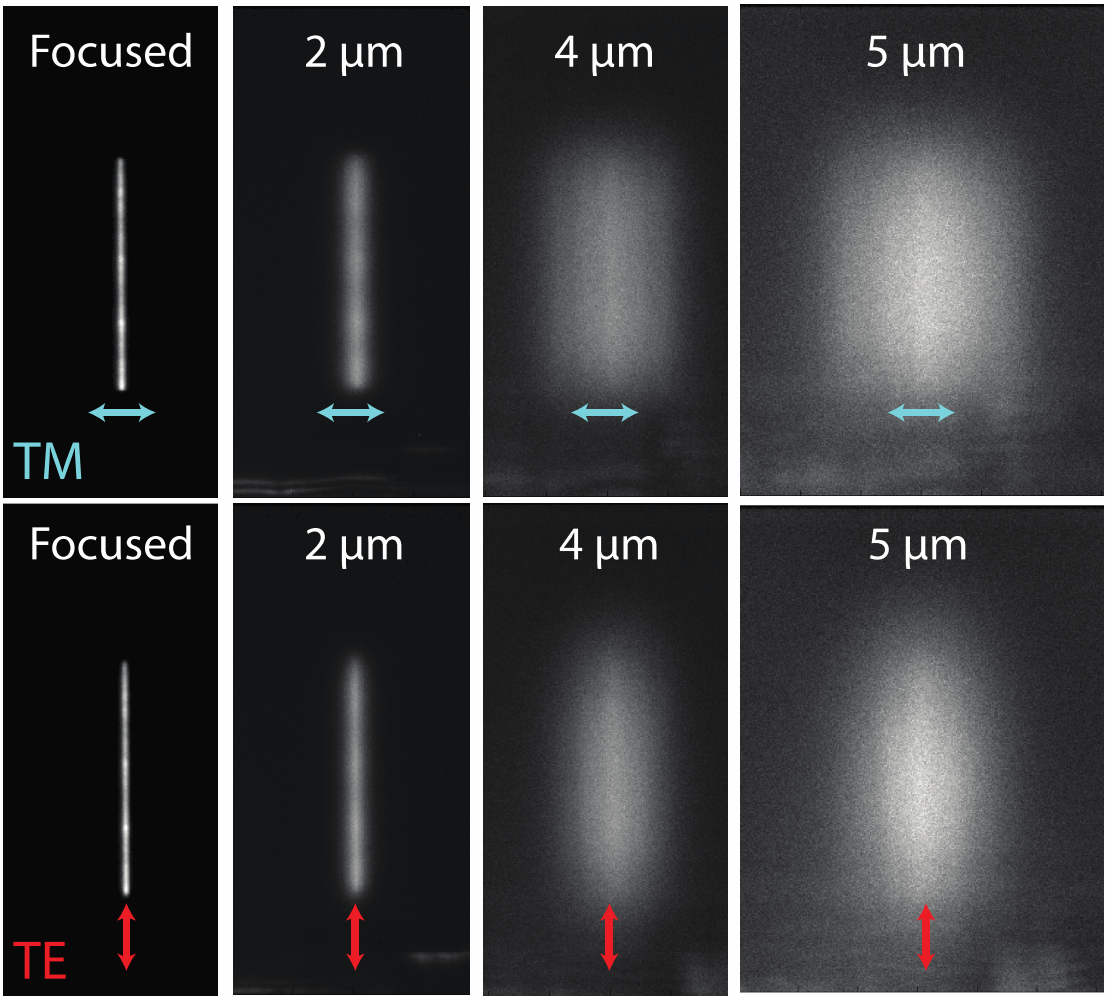

Supplementary Figure S11: TM and TE EL images at various heights above a 20 µm long, 160-nm-wide antenna-electrode on flat QW. Each column corresponds to imaging at 2 µm m, 4 µm and 5 µm above the sample surface. The top and bottom panels show the TM- and TE-polarized EL. Due to the lack of carrier confinement, both TE and TM angular radiation pattern are expected to be the same as that of the bare QW. When the EL is defocused by 5 µm, it is clear that the TM far-field pattern is broader than that of the TE as expected from theoretical calculations. These real space defocused images are corrected by a $\cos(\theta)$ apodization factor to give the radiation intensity as a function of angle.

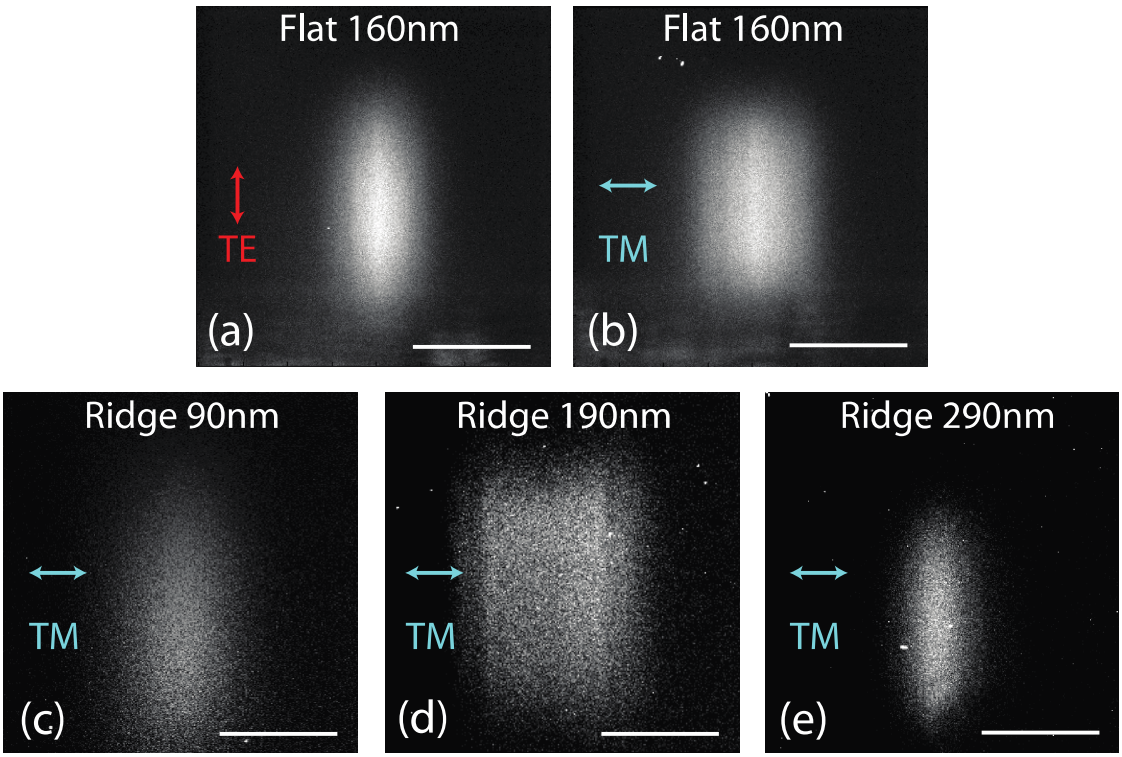

Supplementary Figure S12: 5µm-defocused EL images of different antenna-electrodes designs. a, TE-polarized EL image of 160-nm-wide antenna on flat QW. **b,** TM-polarized EL image of 160-nm-wide antenna on flat QW. **c,** TM-polarized EL image of 90-nm-wide antenna on QW ridge, qualitative the TM lateral spread is similar to the TE pattern. **d,** TM-polarized EL image of 190-nm-wide antenna on QW ridge exhibits two emission lobes at large lateral displacements corresponding to the large angle radiation. **e,** TM-polarized EL image of 290-nm-wide antenna on QW ridge exhibits a narrower emission image than the TE radiation pattern. All scale bars correspond to 20 µm.

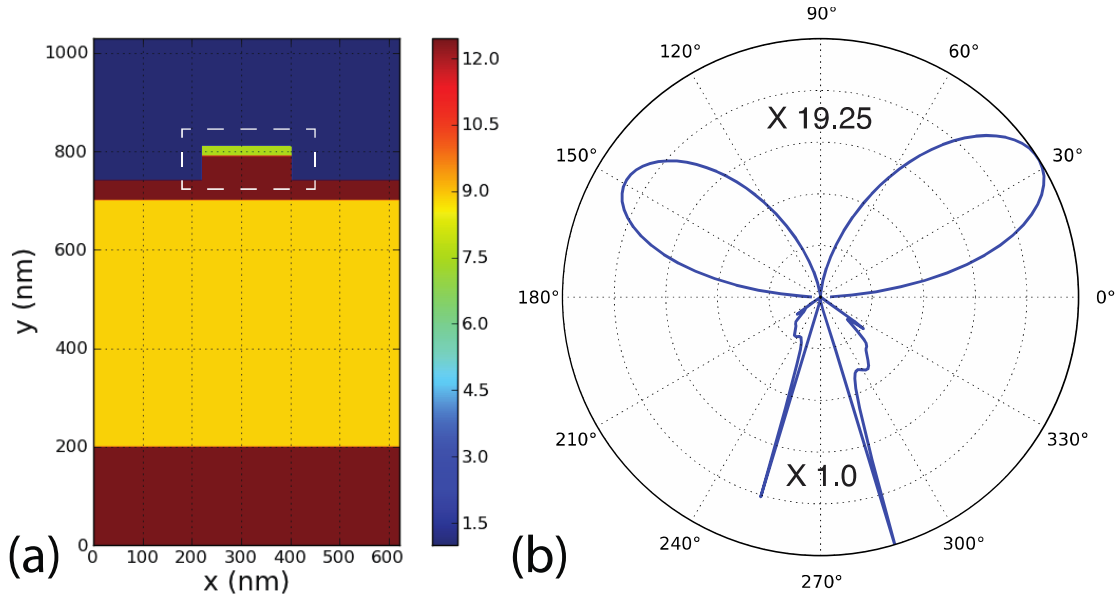

Supplementary Figure S13: Example NTFF calculation. a, Map of simulation relative permittivity. White dashed line indicates the equivalence current surface. **b,** Computed far-field radiation pattern for a vertically oriented-dipole placed 10 nm underneath the left edge of the Au stripe shown in **a**. The radiation intensities in the upper and lower hemisphere are separately normalized to their maximum values. Their relative magnitudes are denoted by the multiplication factors. In the upper hemisphere, the radiation pattern is quadrupolar with a stronger emission lobe towards the right side. This is attributed to the asymmetric excitation of the Au stripe from the left edge. The lower hemisphere exhibits many radiation peaks due to multiple layers of high index substrate. Ensemble radiation pattern for randomly polarized dipoles distributed throughout the entire width of the QW is obtained by summing the polar radiation intensity pattern for each dipole orientation (vertical and horizontal for TM and out of the page for TE) and position (in steps of 4 nm).

Supplementary Discussion

The radiation pattern calculated in a 2D simulation for a 3D structure which is invariant in one of its dimensions in the plane where the azimuthal angle is zero is exactly equivalent to the full 3D simulation. The reason for this is as follows. The 2D simulation can be treated as a 3D simulation where the structure and all field components are invariant in the third dimension. Thus, a current source in 2D is equivalent to a line of identical current sources in 3D. Provided the distance to the observation point (r tends to infinity) is much larger than the spatial extent of the current sources (definition of the far-field approximation), the total contribution of all the current sources for azimuthal angle ϕ=0 as a function of the polar angle will be the same as for a single current source (3D) because all the current sources add in phase, although the absolute radiated power per unit solid angle (radiation intensity) will be different. This can also be understood in terms of the calculation of the radiation pattern for a linear antenna array in the plane where the far-field propagating phase variation between each antenna element is zero[39]. Supplementary Fig. S5 shows the numerical confirmation of the equivalence between the radiation pattern of 2D dipoles simulated in FDTD in conjunction with our near-to-far-field transformation and the exact analytical 3D infinitesimal dipole embedded in a substrate for all three dipole orientations. The radiation in the upper and lower hemispheres is separately normalized to their maximums. The normalization factors are displayed in the respective hemispheres.

Supplementary Methods

Analytical decay rate calculation of an electric dipole near interfaces. The theoretical decay rate enhancement of a dipole near an Au film of finite thickness is calculated using the forced damped harmonic oscillator model developed by Chance, Prock and Silbey[26]. By decomposing the incident fields of an electric dipole into transverse cylindrical waves and vertical planewaves using Sommerfeld's identity, the modification of decay rate can be expressed in terms of the reflected secondary field at the position of the dipole for each transverse wavevector. The generalized system is shown in Supplementary Fig. S1.

For a dipole oriented normal or parallel to the interfaces the decay rate enhancement are given by:

$$b_{\perp,||} = b_0(1 - qZ_{\perp,||}) \tag{S1}$$

$$Z_{\perp} = 1 - \frac{3}{2} Im \int_0^{\infty} \frac{(1 + r_{12}^{||} e^{-i2kd})(1 + r_{13}^{||} e^{-i2ks})}{(1 - r_{12}^{||} r_{13}^{||} e^{-i2k(d+s)})} u^3 \frac{du}{k}$$

$$Z_{||} = 1 - \frac{3}{4} Im \int_0^{\infty} [\frac{\left(1 + r_{12}^{\perp} e^{-i2kd}\right)\left(1 + r_{13}^{\perp} e^{-i2ks}\right)}{(1 - r_{12}^{\perp} r_{13}^{\perp} e^{-i2k(d+s)})} + \frac{(1 - u^2)\left(1 - r_{12}^{||} e^{-i2kd}\right)\left(1 - r_{13}^{||} e^{-i2ks}\right)}{\left(1 - r_{12}^{||} r_{13}^{||} e^{-i2k(d+s)}\right)}] u \frac{du}{k}$$

(S2)

where q is the emitter intrinsic quantum efficiency, $b_{\perp,||}$ is the decay rate enhancements for the perpendicular or parallel dipole, k is the perpendicular wavevector, u is the transverse in-plane wavevector, $r_{12,13}$ is the reflection coefficient for waves traveling from medium 1 towards medium 2 or 3, d is the distance from the emitter to interface between medium 1 and 2, s is the distance from the emitter to the interface between medium 1 and 3.

Finite-difference time-domain (FDTD) decay rate calculations. All FDTD simulations performed in this study use a grid resolution of 1 nm and a 40 nm thick perfectly matched layer absorbing boundary layer. The size of the finite-difference grid is increased until convergence is reached for the simulated quantity of interest, which is typically 100 - 200 nm spacing from the scatterer to the edge of the PML. Integration surfaces for calculating Poynting vector flux are placed no less than 10 grid points from electric dipoles. All simulations are time-stepped until transient responses have decayed (under pulsed-excitation) or until steady-state has been reached (under continuous excitation).

For 3D simulations, the antenna-electrodes are extended into the perfectly matched layer in the y-direction to model infinitely long electrodes with finite widths and thicknesses in the x- and z-directions. For 2D simulations, the TM and TE finite-difference grid automatically assumes no structural or field variation along the y-direction thus k_y=0 (waves propagate only in the XZ-plane). Since the 2D decay rate enhancement simulation of a dipole (more accurately, a line current) near an antenna-electrode does not include contributions of SPP propagating in the y-direction (along the electrode) as opposed to the full 3D simulation, it is also instructive to compare the flat and ridge structure in 2D simulations.

We calculated the spatial and polarization averaged extraction efficiency from the flat and ridge structures by running a separate simulation for each x-, y- or z-dipole placed at each x-position in steps of 4 nm. For each simulation, the total power radiated upwards into air is normalized by the total emitted power from the dipole. The extraction efficiency is ~3.5% for the 60-nm-wide antenna-electrode on flat QW and ~5.1% for the 90-nm-wide ridge device. We estimated the extraction efficiency taking into account Fresnel reflection from a planar GaAs LED[34] to be 1.44% using

$$C_{ext} \approx (1 - (n_s - n_a)^2/(n_s + n_a)^2)(1 - \cos(\theta_c))/2 \quad \text{(S3)}$$

where n_s=3.5 is the substrate index, n_a=1 is the air index and θ_c is the critical angle.

NTFF of arbitrary scatterers on a layered substrate. The NTFF algorithm implemented in this study follows the method developed by Demarest, Huang and Plumb[36] with the exception that the recursive Fresnel equations are replaced with a transfer matrix algorithm. The paper outlines the method for calculating surface equivalence currents and the use of reciprocity theorem to correctly account for the presence of the substrate. It is important to note that as opposed to the coordinate convention used in the paper, for the 2D case where we are only interested in the XZ-plane where the azimuthal angle ϕ=0, we define the TE polarization as the case where the electric field is perpendicular to the plane of incidence and the TM polarization is the case where the magnetic field is perpendicular to the plane of incidence.

In our structure we would like to obtain the radiation pattern for a Au plasmonic stripe resonator sitting on top of a 50-nm-tall GaAs ridge excited by an electric dipole located 10 nm beneath the Au surface (see Supplementary Fig. S13). To perform the NTFF transformation, we identify the scatterer as the 20 nm thick, finite width Au stripe which supports the second SPP resonance and the 50 nm tall, finite width GaAs ridge. The layered media from top to bottom consists of semi-infinite air, 40 nm GaAs, 500 nm $Al_{0.95}Ga_{0.05}As$ and semi-infinite GaAs. Supplementary Fig. S5a shows the relative permittivity distribution used in the FDTD simulation where ε_{GaAs}=12.46, ε_{AlGaAs}=8.85 and ε_{Au} =-35.55-i3.17 (represented by its Lorentz-Drude model fitting parameter ε_{∞}=7.5). We calculate the complex electric and magnetic fields $(\vec{E}, \vec{H})$ around a closed-surface S_{eq} indicated by the dashed white line in 2D FDTD simulations, which are subsequently used to compute the equivalence surface currents given by:

$$\vec{M} = \vec{E} \times \hat{n} \qquad \text{(S4)}$$
$$\vec{J} = \hat{n} \times H$$

where $\vec{M}$ is the magnetic current, $\vec{J}$ is the electric current and $\hat{n}$ is the unit vector normal to the surface.

For each emission angle and polarization (TE or TM) of interest, we calculate the fields at each point on S_{eq} due to the radiation produced by an infinitesimal test current source (TE or TM) placed in the far-field using the transfer matrix method in the absence of the scatterer. Using the reciprocity theorem, the electric far fields $\vec{E}_{ff}^{\vec{J},\vec{M}}$ produced by a near-field infinitesimal electric or magnetic current source ($\vec{J}$ and $\vec{M}$) can be expressed as follows:

$$\vec{E}_{ff,TE}^{\vec{J}} = \frac{1}{I_{TE}d\phi}(\vec{E}_{tx}^{TE}I_x dx + \vec{E}_{ty}^{TE}I_y dy + \vec{E}_{tz}^{TE}I_z dz)$$

$$\vec{E}_{ff,TM}^{\vec{J}} = \frac{1}{I_{TE}d\theta}(\vec{E}_{tx}^{TM}I_x dx + \vec{E}_{ty}^{TM}I_y dy + \vec{E}_{tz}^{TM}I_z dz)$$

$$\vec{E}_{ff,TE}^{\vec{M}} = \frac{1}{K_{TE}d\phi}(\vec{E}_{tx}^{TE}K_x dx + \vec{E}_{ty}^{TE}K_y dy + \vec{E}_{tz}^{TE}K_z dz)$$

$$\vec{E}_{ff,TM}^{\vec{M}} = \frac{1}{K_{TM}d\theta}(\vec{E}_{tx}^{TM}K_x dx + \vec{E}_{ty}^{TM}K_y dy + \vec{E}_{tz}^{TM}K_z dz) \quad \text{(S5)}$$

where $I_x dx, I_y dy, I_z dz$ are the electric dipole moments corresponding to the equivalence surface electric currents, $K_x dx, K_y dy, K_z dz$ are the magnetic dipole moments corresponding to the equivalence surface magnetic currents, $\vec{E}_{t,x,y,z}^{TE,TE}$ are the x,y,z components of the electric field radiated by a TE or TM test dipole $I_{TE}d\phi, I_{TM}d\theta$ at the location of the equivalence surface electric current and $\vec{H}_{t,x,y,z}^{TE,TE}$ are the x,y,z components of the magnetic field radiated by a TE or TM test dipole $K_{TE}d\phi, K_{TM}d\theta$ at the location of the equivalence magnetic surface current.

Angular emission pattern measurement with real space imaging. The polar radiation pattern of the antenna-electrode modified EL are measured by defocusing the microscope setup above the sample surface to allow the real space electric field intensity above the sample to be imaged on the CCD camera. The use of defocused imaging maps the spread of electric field intensity in real space in accordance with the Huygen's principle, thus provides intuitive visualization of the flow of light.

Since we have a single emitting region in the plane perpendicular to the length of the electrode (XZ-plane), we can convert the lateral spread of the EL intensity at some known distance above the sample to radiation intensity as a function of polar angle taking into account the apodization factor and magnification of our imaging system. The advantage of this method compared to Fourier-plane imaging is if there are many emitting objects in the microscope field of view, we can spatially separate the radiation pattern of our antenna of interest provided they are several tens of microns apart. The limitation, on the other hand, is that the angular resolution is limited by the point spread function of the microscope system. This method has been validated and compared against Fourier-plane imaging as well as full-field simulations in our previous studies where the radiation pattern of spatially extended structures are measured[19,40].

Supplementary References

39. Balanis, C. *Antenna theory. Analysis and design* (Wiley, 2005).

40. Verslegers, L. *et al.* Planar lenses based on nanoscale slit arrays in a metallic film. *Nano Lett.* **9**, 235–238 (2009).